Noncollinear commensurate antiferromagnetic structure in metallic $Pr_2PdAl_7Ge_4$

Fei Gao,[1,2,*] Hong-Liang Wang,[3,*] Meiyan Cui,[4,*] Weijun Ren,[1,2,†] Chin-Wei Wang,[5] S. Yano,[5] Xinzhi Liu,[6,7] Zhangzhen He,[4] Bing Li,[1,2,‡] and Zhidong Zhang[1,2]

[1]*Shenyang National Laboratory for Materials Science, Institute of Metal Research, Chinese Academy of Sciences, Shenyang 110016, China*
[2]*School of Materials Science and Engineering, University of Science and Technology of China, Shenyang 110016, China*
[3]*Neutron Scattering Laboratory, Department of Nuclear Physics, China Institute of Atomic Energy, Beijing 102413, China*
[4]*State Key Laboratory of Structural Chemistry, Fujian Institute of Research on the Structure of Matter, Chinese Academy of Sciences, Fuzhou 350002, China*
[5]*National Synchrotron Radiation Research Center, Hsinchu 30077, Taiwan*
[6]*Guangdong Provincial Key Laboratory of Magnetoelectric Physics and Devices, School of Physics, Sun Yat-sen University, Guangzhou 510275, China*
[7]*Center for Neutron Science and Technology, School of Physics, Sun Yat-sen University, Guangzhou 510275, China*

(Received 27 April 2023; revised 28 May 2023; accepted 8 June 2023; published 23 June 2023)

We report the crystal structure, magnetic structure, magnetic properties, electrical- and magnetotransport properties, and heat capacity of the rare-earth transition-metal compound $Pr_2PdAl_7Ge_4$. $Pr_2PdAl_7Ge_4$ crystallizes in the noncentrosymmetric tetragonal structure $P\bar{4}2_1m$ (No. 113) with unit cell parameters $a = 6.0059(3)$ Å and $c = 15.2278(13)$ Å. The Néel temperature T_N of $Pr_2PdAl_7Ge_4$ was determined to be 6 K by the temperature dependences of magnetization, heat capacity, and electrical resistivity. The magnetic-field-induced antiferromagnetic to ferromagnetic transition occurs for magnetic fields H along both the ab plane and the c axis. The electrical resistivity shows a metallic behavior with an upturn at the ordering temperature due to a superzone gap. Negative linear magnetoresistance is observed since the magnetic field increases the order degree of the antiferromagnetic state, reducing the magnetic correlation scattering. Neutron powder diffraction experiments reveal that metallic $Pr_2PdAl_7Ge_4$ has an unusual noncollinear commensurate antiferromagnetic structure with the propagation vector $\boldsymbol{k} = (0,\ 0,\ 0.5)$. Magnetic Pr atom layers stack with the ABBA sequence along the c axis. Within the layers, the Pr moments lie in the ab plane, and the angle between the nearest-neighbor spins is 67.1°. This magnetic structure can well explain the magnetic properties of $Pr_2PdAl_7Ge_4$.

DOI: 10.1103/PhysRevB.107.214435

I. INTRODUCTION

Multicomponent intermetallic compounds containing rare-earth (R) elements are known to show a wide range of unusual behaviors, such as complex magnetism, heavy-fermion superconductivity, non-Fermi-liquid behavior, various ground states, and metamagnetic transitions [1–6], which has raised considerable interest in studying their physical properties. The quasi-two-dimensional rare-earth transition-metal quaternary compounds $CeXAl_4Si_2$ (X = Rh, Ir, and Pt) crystallize in the tetragonal KCu_4S_3-type structure ($P4/mmm$) in which $CeRhAl_4Si_2$ and $CeIrAl_4Si_2$ are moderately heavy fermion antiferromagnets, while $CePtAl_4Si_2$ is a ferromagnet [7–10]. During the exploration of the possible consequences of, e.g., expanding the family by replacing Si with larger Ge, the quasi-two-dimensional compounds $CePtAl_4Ge_2$, $CeAuAl_4Ge_2$, and $Ce_2MAl_7Ge_4$ (M = Ir, Co, Ni, Pd) were discovered [11–15]. $CeAuAl_4Ge_2$ crystallizes in the trigonal structure (space group $R\bar{3}m$, No. 166) and orders antiferromagnetically at 1.4 K [13]. The isostructural Kondo metal $CePtAl_4Ge_2$ exhibits an incommensurate spin density wave with an ordering wave vector $\boldsymbol{k} = (1.39,\ 0,\ 0.09)$ below 2.3 K [11,12]. The recently discovered $Ce_2PdAl_7Ge_4$ crystallizes in a noncentrosymmetric tetragonal structure with space group $P\bar{4}2_1m$ (No. 113), consisting of square net layers of rare-earth atoms separated by Ge-Al and Ge-Al-M-Al-Ge blocks [14,15], which was suggested to be a heavy-fermion compound close to the quantum critical point [15]. Its interesting properties might be related to the specific rare-earth Ce, crystallographic structure, or magnetic structure.

In this work, we grew $Pr_2PdAl_7Ge_4$ single crystals using the self-flux method to expand the study of the family of $R_2PdAl_7Ge_4$ compounds. $Pr_2PdAl_7Ge_4$ orders antiferromagnetically at 6 K. A large magnetic frustration index and the metamagnetic transitions occur at low magnetic fields, suggesting dramatic competition between ferromagnetic (FM) and antiferromagnetic (AFM) couplings. The magnetic structure of $Pr_2PdAl_7Ge_4$ was determined by neutron powder diffraction (NPD) to be a noncollinear commensurate AFM structure, which is rarely seen in metallic compounds.

II. EXPERIMENTAL DETAILS

Single crystals of $Pr_2PdAl_7Ge_4$ were grown using the Al-Ge flux method [16]. High-purity praseodymium chunks, aluminum cylinders, germanium grains, and palladium powders

*These authors contributed equally to this work.
†wjren@imr.ac.cn
‡bingli@imr.ac.cn

with a starting atomic composition of 2:60:40:1 were loaded into a high-quality alumina crucible and sealed in a quartz tube under high vacuum. The mixture was heated to 1273 K and kept for 6 h at this temperature to homogenize the liquid metal, then cooled to 873 K at a rate of 2 K/h. The excess molten liquid flux was separated from the crystals in a centrifuge with silica wool serving as a filter. The obtained single crystals show metallic luster at the surface and have a plateletlike shape with the c axis perpendicular to the plane. A photograph of the $Pr_2PdAl_7Ge_4$ single crystal was taken by an optical microscope (Nikon SMZ745T).

A suitable single crystal was selected and mounted on a glass fiber for single-crystal x-ray diffraction (XRD) measurements. Single-crystal XRD measurements were conducted on an XtaLAB Synergy-S Single Crystal x-ray diffractometer using Cu $K\alpha$ radiation ($\lambda = 1.5418$ Å) at 293 K. The data were refined by direct methods via OLEX2 software using full-matrix least squares fitting on F^2 [17], and the final refined structural parameters were checked using the PLATON program [18]. A Cu $K\alpha$ XRD ($\lambda = 1.5418$ Å, SmartLab, Rigaku) was used for the structure and composition characterization of the powder, and the powder XRD pattern was refined using FULLPROF SUITE software. The (001) surface of the $Pr_2PdAl_7Ge_4$ single crystal was studied with a Bruker D8 3 kW XRD detector using Cu $K\alpha$ radiation ($\lambda = 1.5418$ Å). The chemical composition of the $Pr_2PdAl_7Ge_4$ single crystal was analyzed using a scanning electron microscope (MERLIN Compact, ZEISS) with an energy-dispersive x-ray spectrometer (EDX) at an accelerating voltage of 20 kV and an inductive coupled plasma optical emission spectrometer (5800, Agilent). The $La_2PdAl_7Ge_4$ single crystal was also characterized by EDX and XRD using the same methods.

NPD experiments were performed on $Pr_2PdAl_7Ge_4$ powders using the high-resolution powder diffractometer ECHIDNA with a center wavelength (CW) of 2.439 Å [19] and the multiplexing cold-neutron triple-axis spectrometer SIKA with the wavelength of 3.187 Å ($E_i = E_f = 8.07$ meV) [20,21] at the Open Pool Australian Lightwater (OPAL) reactor, Australian Nuclear Science and Technology Organization (ANSTO). For NPD experiments, 2.1 g of powder samples prepared by grinding $Pr_2PdAl_7Ge_4$ single crystals were loaded in vanadium cans. The diffraction patterns of $Pr_2PdAl_7Ge_4$ were collected with ECHIDNA at 3 and 20 K and with SIKA at 1.5 K. Rietveld refinement of both the magnetic and crystal structures for NPD data was done using the FULLPROF SUITE software [22,23]. The built-in BASIREPS in FULLPROF SUITE and the Bilbao Crystallographic Server [24,25] were employed to identify the magnetic space group, and VESTA software was used to visualize the crystal and magnetic structures.

DC magnetization measurements between 2 and 300 K were performed under magnetic fields up to 70 kOe in the field-cooling (FC) mode using a magnetic property measurement system (XL-7, Quantum Design). Electrical resistivity $\rho(T)$ and heat capacity $C_p(T)$ measurements for $Pr_2PdAl_7Ge_4$ were carried out in a physical property measurement system (Quantum Design) from room temperature down to 2 K. Electrical contacts for electrical resistivity measurements were made using the standard four-wire method with the current along the ab plane, and the 300-μm-diameter Pt wires were attached to the sample with EPO-TEK H20E silver epoxy. Heat capacity was measured using the thermal relaxation technique down to 2 K.

TABLE I. Crystal data and structure refinement for $Pr_2PdAl_7Ge_4$.

Parameter	Value
fw	867.44
T (K)	293(2)
λ (Å)	1.5418
Space group	$P\bar{4}2_1m$
a (Å)	6.0059(3)
c (Å)	15.2278(13)
V (Å^3)	549.28(7)
Z	2
D_{calcd} (g/cm^3)	5.245
μ (mm^{-1})	96.818
Goodness of fit on F^2	1.135
R_1, wR_2 $[I > 2\delta(I)]$[a]	4.99%, 13.32%
R_1, wR_2 (all data)	5.00%, 13.32%

[a]$R_1 = \sum ||F_0|| - ||F_c|| / \sum ||F_x||$, $wR_2 = \{\sum w[(F_0)^2 - (F_c)^2]^2 / \sum w[(F_0)^2]^2\}^{1/2}$.

III. RESULTS AND DISCUSSION

A. Crystal structure

The crystallographic data, atomic coordinates, equivalent isotropic displacement parameters, and anisotropic displacement parameters for $Pr_2PdAl_7Ge_4$ determined by single-crystal XRD at room temperature are presented in Tables I–III. The detailed crystal parameters, including bond lengths and bond angles, are listed in Tables S1–S2 in the Supplemental Material [26]. The Crystal Structure Database (CSD) number we deposited for $Pr_2PdAl_7Ge_4$ is 2218645, and the checkCIF/PLATON report is in the Supplemental Material [26]. $Pr_2PdAl_7Ge_4$ crystallizes in a noncentrosymmetric tetragonal structure with space group $P\bar{4}2_1m$ isostructural to $Ce_2PdAl_7Ge_4$. During the data analysis, we found that the centrosymmetric space group $P4/nmm$ is also close to satisfying the error of refinement. But the error of refinement in the $P4/nmm$ model is much worse than in the $P\bar{4}2_1m$ model;

TABLE II. Atomic coordinates and equivalent isotropic displacement parameters for $Pr_2PdAl_7Ge_4$. U_{eq} is defined as being one third of the trace of the orthogonalized U_{ij} tensor.

Atom	x ($\times 10^4$)	y ($\times 10^4$)	z ($\times 10^4$)	U_{eq} ($\times 10^3$ Å^2)	Wyckoff position
Pr(1)	5000	5000	2386(1)	10(1)	4*d*
Pd(1)	5000	5000	5000	9(1)	2*b*
Ge(1)	0	5000	2952(2)	11(1)	2*c*
Ge(2)	0	5000	6911(2)	11(1)	2*c*
Ge(3)	2798(3)	7798(3)	9142(2)	14(1)	4*e*
Al(1)	2429(5)	2571(5)	4096(9)	13(2)	4*e*
Al(2)	7430(5)	7570(5)	5892(8)	14(2)	4*e*
Al(3)	0	5000	8578(4)	13(2)	2*c*
Al(4)	2015(7)	7015(7)	744(3)	9(1)	4*e*

TABLE III. Anisotropic displacement parameters ($\times 10^3$ Å^2) for $Pr_2PdAl_7Ge_4$. The anisotropic displacement factor exponent takes the form $-2\pi^2[h^2a^{*2}U_{11} + \cdots + 2h\,k\,a^*\,b^*\,U_{12}]$.

Atom	U_{11}	U_{22}	U_{33}	U_{23}	U_{13}	U_{12}
Pr(1)	7(1)	7(1)	16(1)	0	0	0(1)
Pd(1)	6(1)	6(1)	17(1)	0	0	0
Ge(1)	8(1)	8(1)	18(1)	0	0	0(2)
Ge(2)	9(1)	9(1)	15(1)	0	0	0(2)
Ge(3)	12(1)	12(1)	20(1)	−2(1)	−2(1)	−1(1)
Al(1)	10(2)	10(2)	19(4)	0(1)	0(1)	−4(3)
Al(2)	13(2)	13(2)	15(4)	1(1)	−1(1)	1(3)
Al(3)	10(2)	10(2)	18(3)	0	0	−1(3)
Al(4)	6(1)	6(1)	15(2)	0(2)	0(2)	−4(2)

the chemical formula obtained from the refinement of the $P4/nmm$ model does not agree with the microscopic composition data, as discussed below. Furthermore, the thermal displacement parameters are unstable and nearly nonpositive definite in $P4/nmm$. All evidence suggests that $P\bar{4}2_1m$ is the correct space group. A similar situation also occurs in $Ce_2PdAl_7Ge_4$ [15], and our results provide further evidence that $R_2PdAl_7Ge_4$ crystallizes in the $P\bar{4}2_1m$ space group.

As shown in Fig. 1(a), a unit cell of $Pr_2PdAl_7Ge_4$ consists of 2 f.u. The crystallographically equivalent Pr atoms occupy the 4*d* (0.5, 0.5, 0.23857) Wyckoff position of low site symmetry 2*z* (C_2 point group; see Figs. 1(b) and 1(c) and Table S1 in the Supplemental Material [26]). The Pd atoms are also crystallographically equivalent, residing in the 2*b* (0.5, 0.5, 0.5) Wyckoff position of the $\bar{4}$ site symmetry. The actual coordination by two types of Al ions is close to the cubic one. There are three crystallographically inequivalent Ge sites, where Ge1, Ge2, and Ge3 occupy the 2*c* (0, 0.5, 0.2952), 2*c* (0, 0.5, 0.69106), and 4*e* (0.2798, 0.7798, 0.91424) Wyckoff positions and Al1, Al2, Al3, and Al4 occupy the 4*e* (0.2429, 0.2571, 0.4096), 4*e* (0.743, 0.757, 0.5892), 2*c* (0, 0.5, 0.8578), and 4*e* (0.2015, 0.7015, 0.0744) Wyckoff positions, respectively. Thus, the crystal structure consists of a planar square net of Pr atoms separated by Ge-Al-Pd-Al-Ge and Al-Ge layers alternating along the *c* axis, and there are four nearest Al-Ge pentahedra neighbors and two nearest Al-Ge tetrahedra neighbors around each Pr atoms. Note that the Al-Ge pentahedra are of different sizes. In a unit cell, the distances between the two nearest Pr atoms are 7.9620(19) Å along the *c* axis and 4.2468(2) Å within the *ab* plane, and the lattice constants obtained are $a = b = 6.0059(3)$ Å and $c = 15.2278(13)$ Å. The powder XRD pattern shown in Fig. 1(d) was collected at 300 K on crushed single crystals. Rietveld refinement results reveal that the crystals are single phase with the $P\bar{4}2_1m$ space group, and the errors of the profile factor $R_P = 8.50\%$, the errors of the weighted profile factor $R_{WP} = 11.20\%$, and the reduced χ^2 is $\chi^2 = 3.26$. The (001) plane was identified by XRD on the big facet with a flat surface of the crystal, as shown in Fig. 1(e). The inset of Fig. 1(e) shows a photograph of the thin sheetlike single crystal with dimensions of $3 \times 3 \times 0.5$ mm^3. The atomic percentage of $Pr_2PdAl_7Ge_4$ was determined to be Pr, Pd, Al, Ge = 14.97, 7.19, 49.79, 28.06, which is fully consistent with the composition of Pr:Pd:Al:Ge = 2:1:7:4. Furthermore, the elemental mapping images taken on a $Pr_2PdAl_7Ge_4$ single crystal are shown in Figs. 1(f)–1(i), which confirm that Pr, Pd, Al, and Ge elements uniformly distribute throughout the entire image area.

B. Magnetic properties

Usually, Pr-based intermetallic compounds are ordered magnetically, and the exchange coupling between Pr

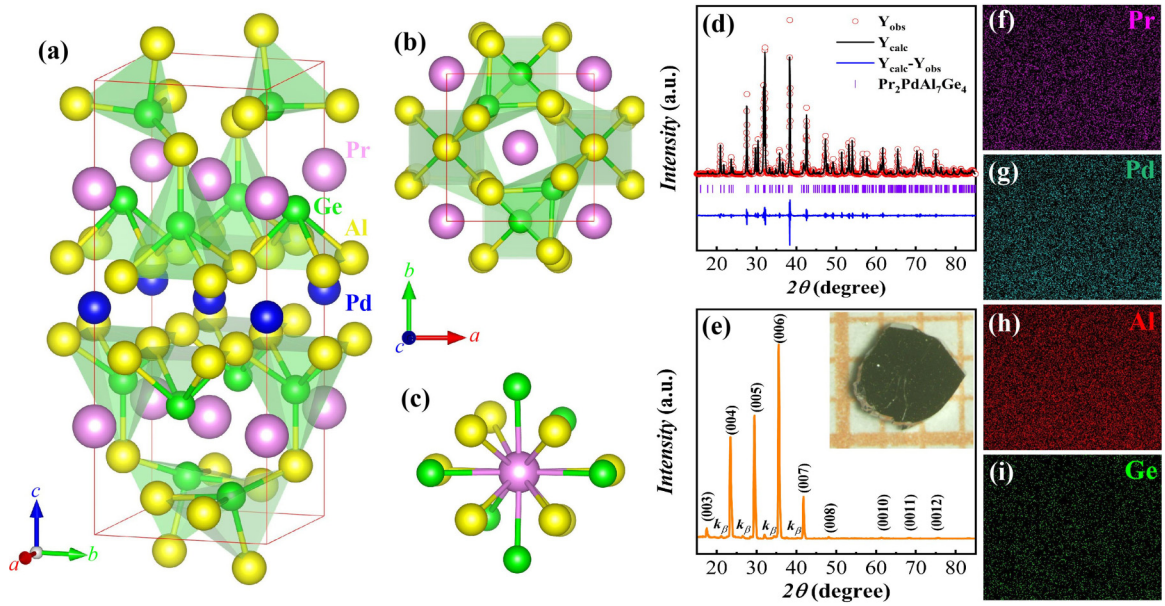

FIG. 1. (a) Crystal structure of $Pr_2PdAl_7Ge_4$. Red lines represent the unit cell. (b) The crystal structure of the (001) plane. (c) Atom environment of Pr. (d) XRD pattern of $Pr_2PdAl_7Ge_4$ powders (ground from single crystals) refined with the Rietveld method. (e) The XRD pattern of a flat facet was identified to be the (001) plane of the $Pr_2PdAl_7Ge_4$ single crystal. The inset shows the photograph of a single crystal on a 1 × 1 mm^2 grid. Elemental mapping images for (f) Pr, (g) Pd, (h) Al, and (i) Ge elements.

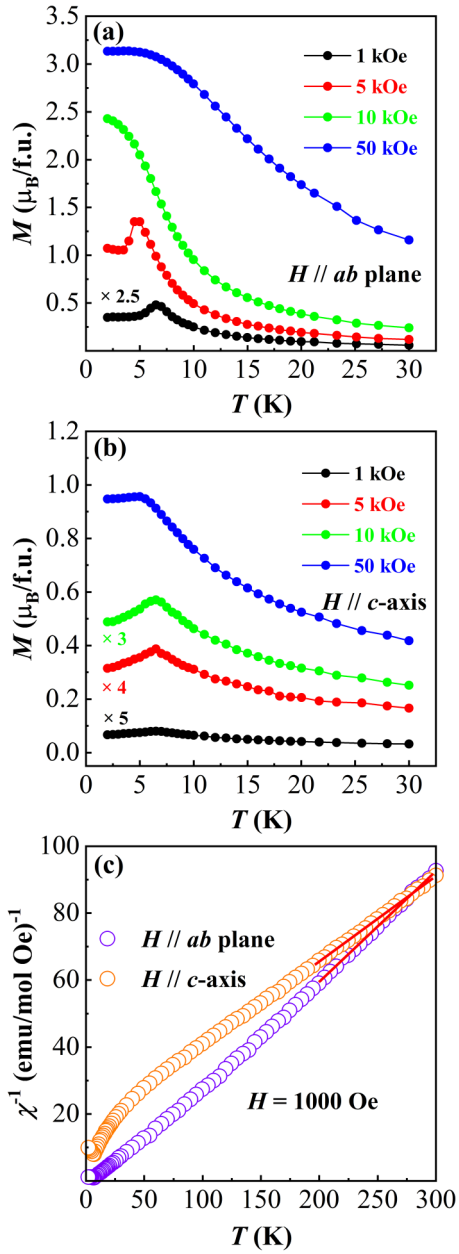

FIG. 2. Temperature dependences of the FC magnetization measured with various external magnetic fields $H = 1$, 5, 10, and 50 kOe for (a) the $H \parallel ab$ plane and (b) the $H \parallel c$ axis in $Pr_2PdAl_7Ge_4$. (c) Temperature dependence of inverse susceptibility $\chi^{-1}(T)$ with an applied magnetic field of 1000 Oe for $H \parallel ab$ plane and $H \parallel c$ axis. The solid line represents a Curie-Weiss fit to the data.

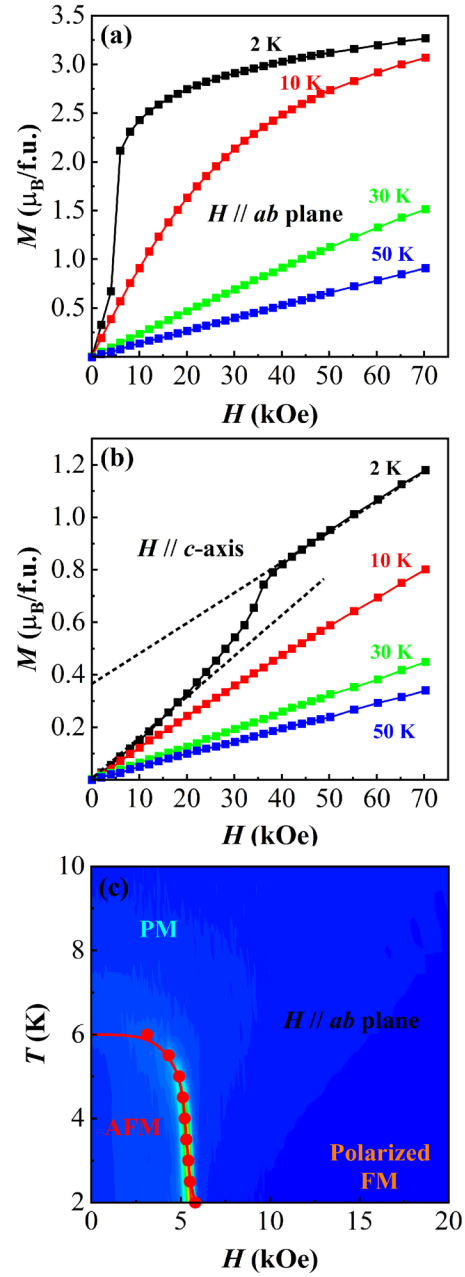

FIG. 3. Magnetization M plotted as a function of magnetic field H of $Pr_2PdAl_7Ge_4$ for (a) $H \parallel ab$ plane and (b) $H \parallel c$ axis in the temperature range 2–50 K. (c) Magnetic phase diagram for $H \parallel ab$ plane.

magnetic moments is dominated by indirect RKKY exchange interactions [27]. The temperature-dependent magnetization $M(T)$ of $Pr_2PdAl_7Ge_4$ measured in applied magnetic fields H of 1–50 kOe are shown in Figs. 2(a) and 2(b). The peaks appear at 6 K in the $M(T)$ curves for a magnetic field of 1 kOe applied both along the ab plane ($H \parallel ab$ plane) and the c axis ($H \parallel c$ axis), suggesting an AFM transition temperature of $T_N = 6$ K. The absence of peaks in the curves for $H \parallel ab$ plane when $H = 10$ and 50 kOe is because these two magnetic fields are larger than the critical field of a metamagnetic transition for $H \parallel ab$ plane [see the discussion of Fig. 3(a) below]; the paramagnetic (PM) to AFM transition changes to a PM to FM transition of $M(T)$. Temperature dependences of inverse magnetic susceptibility $\chi^{-1}(T) = \frac{H}{M(T)}$ are represented in Fig. 2(c); the Curie-Weiss formula $\chi(T) = \frac{C}{T-\theta_{CW}}$ is used to fit the data above 200 K, where $C = N_A\mu_{eff}^2/3k_B$ is the Curie constant, N_A is Avogadro's number, and k_B is the Boltzmann constant [28]. It reveals a Curie-Weiss temperature of $\theta_{CW} = 22$ K for $H \parallel ab$ plane and $\theta_{CW} = -62$ K for $H \parallel c$ axis. The negative Curie-Weiss temperatures for $H \parallel c$ axis indicate the dominance of the AFM interaction. The large magnetic anisotropy in the

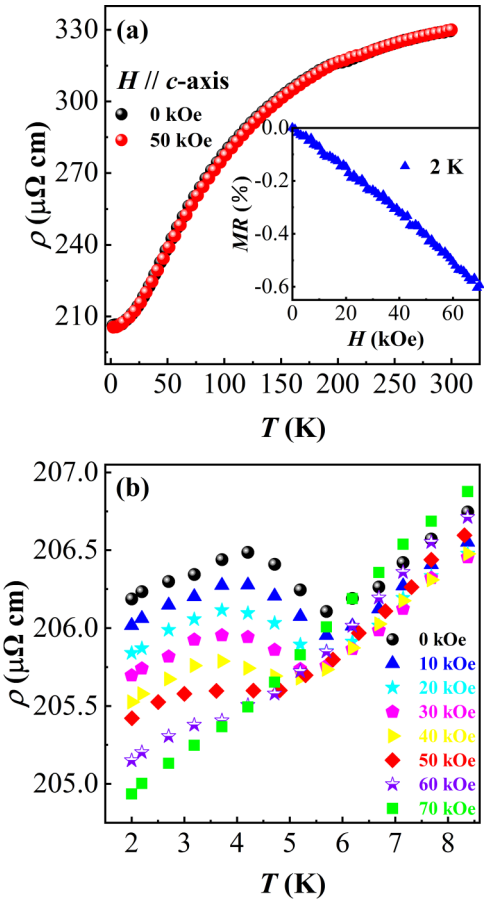

FIG. 4. (a) Temperature dependences of the electrical resistivity measured at zero magnetic fields and a magnetic field of 50 kOe applied along the c axis of $Pr_2PdAl_7Ge_4$. The inset shows the field dependence of MR at 2 K for $Pr_2PdAl_7Ge_4$. (b) Temperature-dependent electrical resistivity of $Pr_2PdAl_7Ge_4$ at various magnetic fields below 9 K.

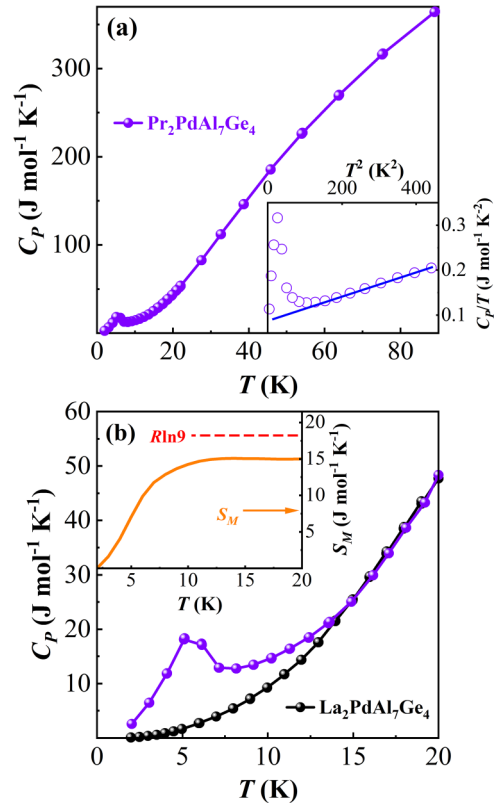

FIG. 5. (a) Temperature-dependent heat capacity of $Pr_2PdAl_7Ge_4$. The inset displays the relationship curve between $C_P(T)/T$ and T^2 at low temperatures and its fitting curve. The blue solid line is a fit to the data using the described low-temperature Debye model. (b) Temperature dependences of heat capacity for $La_2PdAl_7Ge_4$ and $Pr_2PdAl_7Ge_4$. The inset shows the temperature evolution of the magnetic contribution to the entropy S_M of $Pr_2PdAl_7Ge_4$.

paramagnetic state of $Pr_2PdAl_7Ge_4$ may be ascribed to the crystal electric field (CEF) effect. The frustration index $f = |\theta_{CW}/T_N|$ is ~10, implying the strong magnetic frustration of $Pr_2PdAl_7Ge_4$ originates from the competition between FM and AFM exchange interactions of the nearest and high-order neighboring Pr-Pr atoms due to the oscillating RKKY interaction. The obtained effective moment μ_{eff} for $H \parallel ab$ plane is $3.46\mu_B$/f.u., close to the theoretical value for the Pr^{3+} ion in the $^3H_4$ ground state $g_J\sqrt{J(J+1)}\mu_B = 3.58\ \mu_B$, with $J = 4$ and $g_J = 4/5$.

The magnetization curves $M(H)$ of $Pr_2PdAl_7Ge_4$ at 2, 10, 30, and 50 K with applied magnetic fields up to 70 kOe for $H \parallel ab$ plane and for $H \parallel c$ axis are plotted in Figs. 3(a) and 3(b). The 2 K $M(H)$ for $H \parallel ab$ plane is almost linear when $H < 6$ kOe, and then a magnetization jump occurs due to a field-induced spin-flip transition at a critical field of ~6 kOe. The metamagnetic transition in $Pr_2PdAl_7Ge_4$ implies a noncoherent rotation of the magnetic moments, and the magnetic behavior can be well understood by its specific magnetic structure, as discussed below. At a high magnetic field, magnetization approaches saturation, and the saturation value obtained by using an Arrott plot (M^2 versus H/M, not shown) is $2.54\mu_B$/Pr, smaller than the theoretical value of $g_J J = 3.20\mu_B$. The $M(H)$ curve at 2 K for $H \parallel c$ axis consists of two lines due to a field-induced transition that occurred at $H \sim 22$ kOe. The upper line does not pass through the origin point, indicating that it is not an $M(H)$ for a certain crystallographic direction of the AFM compound. Thus, this metamagnetic transition is not a pure spin-flop type but a composite of spin flop and spin flip. The nonlinear $M(H)$ curve at 10 K for $H \parallel ab$ plane results from the short-range order several degrees above T_N. The linear $M(H)$ curves in Figs. 3(a) and 3(b) are consistent with the PM state of $Pr_2PdAl_7Ge_4$. The magnetic phase diagram with the phase boundaries for $H \parallel ab$ plane was obtained with the differential magnetization (dM/dH) at different temperatures, as shown in Fig. 3(c). With increasing temperatures, the AFM ground state gradually evolves into a PM state.

C. Electrical resistivity

The electrical resistivity of $Pr_2PdAl_7Ge_4$ recorded at zero magnetic field and a field of 50 kOe is displayed as a function of temperature in Fig. 4(a), where the electrical current was

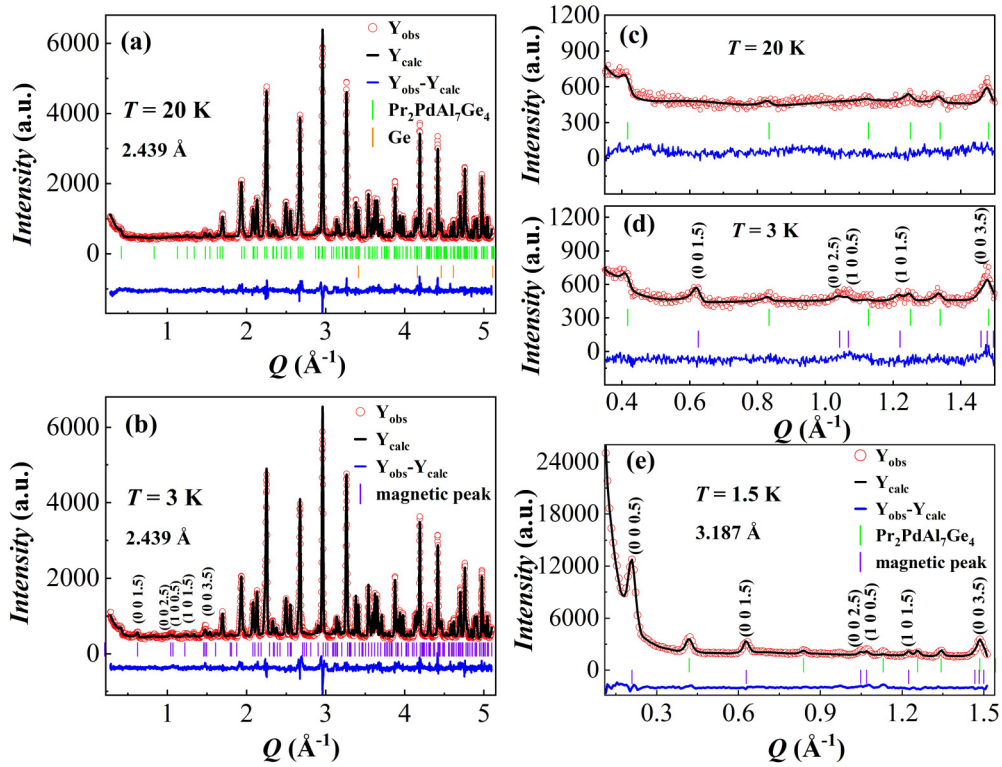

FIG. 6. Rietveld refinement results of the NPD patterns for $Pr_2PdAl_7Ge_4$ at (a) 20 K $>$ T_N and (b) 3 K $<$ T_N collected in ECHIDNA for 2.439 Å. (c) and (d) show part of the diffraction pattern for 20 and 3 K neutron data, indicating the additional magnetic reflections upon cooling. (e) Rietveld refinement of the NPD patterns of $Pr_2PdAl_7Ge_4$ at 1.5 K $<$ T_N in SIKA with a neutron wavelength of 3.187 Å. The experimental data and calculated pattern are shown as open red circles and solid black lines. The blue lines at the bottom show the difference between the measured and calculated intensities. The green and violet vertical bars indicate the nuclear and magnetic Bragg peaks. The orange vertical bars represent the Ge impurity peaks.

applied along the *ab* plane and the magnetic field was applied along the crystalline *c* axis. Overall, electrical resistivity decreases with decreasing temperature, showing a metallic behavior. It is weakly temperature dependent above 150 K; with a decrease in temperature, a broad "knee" appears at around 50–150 K, similar to that of $Ce_2PdAl_7Ge_4$ [15]. Although both the scattering rate and itinerant carrier density decrease with decreasing temperature, the competition between them could lead to such a broad knee. As seen in Fig. 4(b), electrical resistivity shows an upturn at the ordering temperature of 6 K. This type of electrical resistivity increase at the magnetic ordering temperature is due to the formation of a magnetic superzone gap when the magnetic periodicity is greater than the lattice periodicity [29]. The superzone gap is usually observed in heavy rare-earth metals and rare-earth intermetallic compounds [30], and the presence of a superzone gap was also reported for UCu_2Sn, $CePd_5Al$, CeGe, $PrIr_3B_2$, $SmFe_2Al_{10}$, Ho_7Rh_3, and RAl_2Ge_2 [31–38]. At lower temperatures, the electrical resistivity decreases with decreasing temperature, which is attributed to the reduction in spin disorder scattering in the long-range magnetically ordered state. The magnetoresistance (MR), defined as $\{[\rho(H) - \rho(0)]/\rho(0)\} \times 100\%$, was measured up to 70 kOe. A negative linear MR is observed, as shown in the inset of Fig. 4(a), since the magnetic field increases the order degree of the AFM state and thus reduces the magnetic correlation scattering. At 2 K, the MR is -0.6% for a magnetic field of 70 kOe.

D. Heat capacity

The heat capacity $C_P(T)$ of $Pr_2PdAl_7Ge_4$ measured in the absence of the magnetic field is shown in Fig. 5(a). C_P decreases monotonically with decreasing temperature and exhibits a λ-shaped peak at T_N for the compound. In the inset in Fig. 5(a), the data from 10 to 20 K can be well fitted by the low-temperature Debye model using the expression $C_P(T)/T = \gamma + \beta T^2$, where γ is the electron contribution of the heat capacity and βT^2 is the low-temperature limit of the lattice term [39]. The fit yields $\beta = 3.544 \times 10^{-4}$ J mol^{-1} K^{-4} and $\gamma = 0.035$ J mol^{-1} K^{-2}, and the Debye temperature calculated from β using the relation $\Theta_D = (12\pi^4 NR/5\beta)^{1/3}$ (where R is the number of atoms in the formula unit) is 424 K. In Fig. 5(b), we estimate the $4f$-derived contribution to the magnetic entropy of $Pr_2PdAl_7Ge_4$ by integrating $C_P(T)/T$ data after subtracting the heat capacity of nonmagnetic $La_2PdAl_7Ge_4$, assuming the lattice contribution to C_P of $Pr_2PdAl_7Ge_4$ is identical to that of $La_2PdAl_7Ge_4$. The magnetic entropy of $Pr_2PdAl_7Ge_4$ recovers to 15.09 J mol^{-1} K^{-1} at 15 K, reaching ~83% of $R\ln(2J + 1) = R\ln 9 = 18.27$ J mol^{-1} K^{-1}, with $J = 4$. This indicates an influential effect of the CEF on the Pr^{3+} ions.

E. Neutron powder diffraction and magnetic structure

To determine the magnetic structure of $Pr_2PdAl_7Ge_4$, NPD experiments were carried out at ECHIDNA and SIKA of

TABLE IV. The magnetic mode of $Pr_2PdAl_7Ge_4$.

Coordinates of Pr	m_x	m_y	m_z	m
x, y, z	1.030	0.683	0	1.236
$-x+1/2, y+1/2, 1-z$	−1.030	0.683	0	1.236
$y, -x, 1-z$	−1.030	−0.683	0	1.236
$y+1/2, x+1/2, z$	1.030	−0.683	0	1.236

ANSTO. Figure 6(a) illustrates the diffraction pattern of ECHIDNA measured with a CW of 2.439 Å at 20 K. It corresponds well to the high-temperature crystal symmetry, indicating no structural transition occurs from room temperature to 20 K. Figure 6(b) represents a diffraction pattern measured at 3 K with a neutron wavelength of 2.439 Å, in which the additional Bragg peaks appear due to long-range magnetic order. The position of the magnetic peaks can be clearly seen in the partially enlarged diffraction pattern [Figs. 6(c) and 6(d)]. Figure 6(e) is the diffraction pattern measured by SIKA at 1.5 K with a longer neutron wavelength of 3.187 Å; the position of magnetic peaks corresponds very well to those in Fig. 6(b). BASIREPS of FULLPROF SUITE [23,40] and MAXMAGN of the Bilbao Crystallographic Server [23,24] were employed to determine the magnetic structure of $Pr_2PdAl_7Ge_4$. All the magnetic peaks can be indexed with a commensurate ordering wave vector $\boldsymbol{k} = (0,\ 0,\ 0.5)$. The strong magnetic peaks (0 0 0.5) and (0 0 1.5) imply that the majority of the magnetic moments lie in the *ab* plane. The best-fitting magnetic mode of the Pr(4d) site with propagation vector $\boldsymbol{k} = (0,\ 0,\ 0.5)$ is represented in Table IV; m_x, m_y, and m_z are the components of the Pr magnetic moment along the x, y, and z axes, respectively, and m is the total magnetic moment. The magnetic space group $P_c2_12_12_1$ (BNS No. 19.28) is identified as providing the best agreement after testing all the possible models one by one against the data using FULLPROF SUITE. The magnetic structure of $Pr_2PdAl_7Ge_4$ is visualized in Fig. 7, where magnetic moments are shown by violet arrows. Along the c axis, there are four magnetic layers of Pr atoms ABBA stacking in a magnetic unit cell. The magnetic moment of each Pr atom is $1.236\mu_B$/Pr and lies in the *ab* plane, the tilting angle between the magnetic moments of the nearest Pr atoms in either the A or B layer was calculated to be 67.1°, and the net magnetic moments of the A and B layers are equal in magnitude and opposite in direction. The magnetic structure can be explained with a Hamiltonian containing in-plane spin anisotropy and competing FM (J_2, J_{c2}) and AFM (J_1, J_{c1}) interactions within the plane and interplane. The strong competition between the in-plane AFM nearest-neighbor (J_1) and FM next-nearest-neighbor (J_2) interactions can explain the emergence of a tilting angle between the nearest-neighbor Pr moments in either the A or B layer. In addition, the interlayer interactions are also AFM (J_{c1}) and FM (J_{c2}) alternately along the c axis, which explains the ABBA stacking feature of the magnetic structure. Furthermore, this noncollinear magnetic structure stems from the CEF effect of the specific crystal structure of $Pr_2PdAl_7Ge_4$. As shown in Fig. 7(c), the local chemical environment, as well as the orientation of the Al-Ge polyhedra of each Pr atom, is different. For example, the orientation of the polyhedra of Pr atoms in layer A is opposite

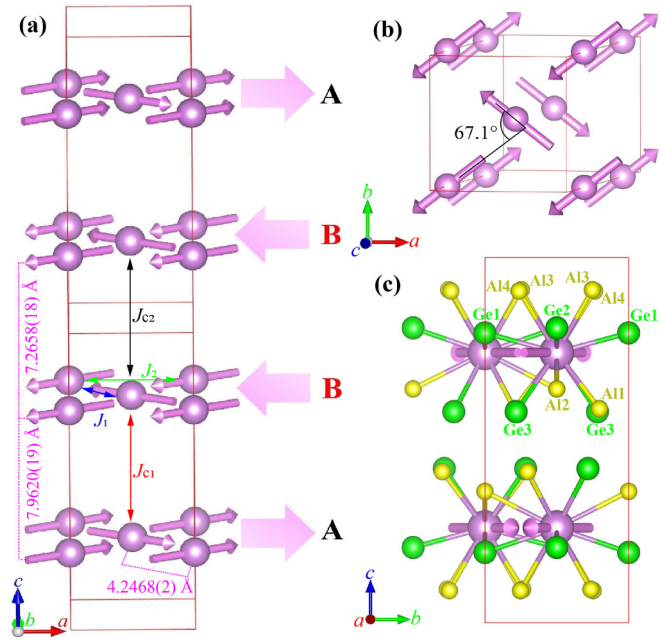

FIG. 7. (a) and (b) The schematic of the determined commensurate noncollinear magnetic structure of $Pr_2PdAl_7Ge_4$. J_1 and J_2 represent the nearest-neighbor AFM and next-nearest-neighbor FM interactions, respectively. J_{c1} and J_{c2} represent the interlayer AFM and FM interactions, respectively. Atoms other than Pr have been removed for clarity. (c) Part of the local chemical environment of the Pr atom in the A (down) and B (up) layers. The pink vectors indicate the magnetic moments of Pr, lying in the *ab* plane with a tilting angle of 67.1° between the nearest-neighbor magnetic moments. Red lines represent the crystal unit cell.

to that in layer B. The different local CEFs cause the different directions of the Pr moments. Similar noncollinear magnetic structures were found in some members of the multiferroic rare-earth perovskite family RMO_3 (M = Sc, Al, and Co), which have a commensurate magnetic structure with Ising-like antiferromagnetism [4,41–46]. The AFM ground state $AxGy$ of RMO_3 is stabilized by the dipole-dipole interaction, and the tilting angle in RMO_3 depends on the relative distortion of the eight Al-O octahedra around R^{3+} [4,45,46]. The occurrence of such magnetic structures in intermetallic compounds is rarely seen.

$Pr_2PdAl_7Ge_4$ is the first compound with the recently discovered $R_2PdAl_7Ge_4$-type structure whose magnetic structure has been determined using the neutron powder diffraction technique. The noncollinear antimagnetic structure can well explain the magnetic properties in Figs. 3(a) and 3(b). Under the same magnetic field, the magnetization for $H \parallel ab$ plane is larger than that for $H \parallel c$ axis, reflecting the strong in-plane anisotropy. The critical magnetic field of 6 kOe for the field-induced magnetic phase transition for $H \parallel ab$ plane is smaller than that of 22 kOe for $H \parallel c$ axis, which is consistent with $|J_2| > |J_{c2}|$. At 6 kOe, the angle between the nearest-neighbor Pr moments in plane was changed by the magnetic field, while the angle between net magnetizations of A and B layers was quickly reduced. Thus, the magnetization jump at the metamagnetic transition is larger than the net magnetizations of the A or B layer.

IV. CONCLUSION

To summarize, we grew a $Pr_2PdAl_7Ge_4$ single crystal using the self-flux method. The compound crystallizes in the noncentrosymmetric tetragonal structure (space group $P\bar{4}2_1m$, No. 113) with lattice parameters $a = 6.0059(3)$ Å and $c = 15.2278(13)$ Å. T_N of $Pr_2PdAl_7Ge_4$ was determined to be 6 K by the temperature dependence of magnetization and further verified by electrical resistivity and heat capacity anomalies at this temperature. At 2 K, a magnetic-field-induced AFM to FM transition occurs at 6 kOe for $H \parallel ab$ plane and 22 kOe for $H \parallel c$ axis. The electrical resistivity rises at the magnetic ordering temperature, implying the presence of a magnetic superzone gap in $Pr_2PdAl_7Ge_4$ below T_N due to the magnetic periodicity being larger than the lattice periodicity. NPD experiments revealed that $Pr_2PdAl_7Ge_4$ is a noncollinear AFM compound (magnetic space group $P_c2_12_12_1$, BNS No. 19.28) with commensurate ordering wave vector $\boldsymbol{k} = (0, 0, 0.5)$, and the Pr moment lies in the *ab* plane with a magnitude of 1.236 μ_B; the angle between the nearest-neighbor Pr spins is 67.1°. The magnetic properties of $Pr_2PdAl_7Ge_4$ can be well understood with this noncollinear magnetic structure.

ACKNOWLEDGMENTS

This work was supported by the Ministry of Science and Technology of China (Grants No. 2021YFB3501201 and No. 2020YFA0406002) and the National Natural Science Foundation of China (Grants No. 52071323 and No. 22205234). We acknowledge the high-resolution powder diffractometer ECHIDNA and the multiplexing cold-neutron triple-axis spectrometer SIKA of the Australian Nuclear Science and Technology Organization for neutron beam time.

[1] T. Kurumaji, T. Nakajima, M. Hirschberger, A. Kikkawa, Y. Yamasaki, H. Sagayame, H. Nakao, Y. Taguchi, T.-H. Arima, and Y. Tokura, Skyrmion lattice with a giant topological Hall effect in a frustrated triangular lattice magnet, Science **365**, 914 (2019).

[2] K. Zhao, H. Deng, H. Chen, K. A. Ross, V. Petrǧíček, G. Günther, M. Russina, V. Hutanu, and P. Gegenwart, Realization of the kagome spin ice state in a frustrated intermetallic compound, Science **367**, 1218 (2020).

[3] X. Y. Tan, V. O. Garlea, K. Kovnir, C. M. Thompson, T. S. Xu, H. B. Cao, P. Chai, Z. P. Tener, S. S. Yan, P. Xiong, and M. Shatruk, Complex magnetic phase diagram with multistep spin-flop transitions in $La_{0.25}Pr_{0.75}Co_2P_2$, Phys. Rev. B **95**, 024428 (2017).

[4] L. S. Wu, S. E. Nikitin, M. Frontzek, A. I. Kolesnikov, G. Ehlers, M. D. Lumsden, K. A. Shaykhutdinov, E.-J. Guo, A. T. Savici, Z. Gai, A. S. Sefat, and A. Podlesnyak, Magnetic ground state of the Ising-like antiferromagnet $DyScO_3$, Phys. Rev. B **96**, 144407 (2017).

[5] H. Shishido, R. Settai, S. Araki, T. Ueda, Y. Inada, T. C. Kobayashi, T. Muramatsu, Y. Haga, and Y. Onuki, Evolution of pressure-induced heavy fermion state and superconductivity in $CeRhIn_5$: A high-pressure Fermi surface study, Phys. Rev. B **66**, 214510 (2002).

[6] V. H. Tran, D. Kaczorowski, R. T. Khan, and E. Bauer, Superconductivity and non-Fermi-liquid behavior of Ce_2PdIn_8, Phys. Rev. B **83**, 064504 (2011).

[7] N. J. Ghimire, F. Ronning, D. J. Williams, B. L. Scott, Y. K. Luo, J. D. Thompson, and E. D. Bauer, Investigation of the physical properties of the tetragonal $CeMAl_4Si_2$ (M = Rh, Ir, Pt) compounds, J. Phys.: Condens. Matter **27**, 025601 (2015).

[8] J. Gunasekera, L. Harriger, A. Dahal, A. Maurya, T. Heitmann, S. M. Disseler, A. Thamizhavel, S. Dhar, D. J. Singh, and D. K. Singh, Electronic nature of the lock-in magnetic transition in $CeXAl_4Si_2$, Phys. Rev. B **93**, 155151 (2016).

[9] A. Maurya, R. Kulkarni, A. Thamizhavel, D. Paudyal, and S. K. Dhar, Kondo lattice and antiferromagnetic behavior in quaternary $CeTAl_4Si_2$ (T = Rh, Ir) single crystals, J. Phys. Soc. Jpn. **85**, 034720 (2016).

[10] N. J. Ghimire, S. Calder, M. Janoschek, and E. D. Bauer, Magnetic structure of the antiferromagnetic Kondo lattice compounds $CeRhAl_4Si_2$ and $CeIrAl_4Si_2$, J. Phys.: Condens. Matter **27**, 245603 (2015).

[11] S. Shin, P. F. S. Rosa, F. Ronning, J. D. Thompson, B. L. Scott, S. Y. Lee, H. Jang, S.-G. Jung, E. Yun, H. Lee, E. D. Bauer, and T. Park, Synthesis and characterization of the heavy-fermion compound $CePtAl_4Ge_2$, J. Alloys Compd. **738**, 550 (2018).

[12] S. Shin, V. Pomjakushin, L. Keller, P. F. S. Rosa, U. Stuhr, C. Niedermayer, R. Sibille, S. Toth, J. Kim, H. Jang, S.-K. Son, H.-O. Lee, T. Shang, M. Medarde, E. D. Bauer, M. Kenzelmann, and T. Park, Magnetic structure and crystalline electric field effects in the triangular antiferromagnet $CePtAl_4Ge_2$, Phys. Rev. B **101**, 224421 (2020).

[13] S. Zhang, N. Aryal, K. Huang, K.-W. Chen, Y. Lai, D. Graf, T. Besara, T. Siegrist, E. Manousakis, and R. E. Baumbach, Electronic structure and magnetism in the layered triangular lattice compound $CeAuAl_4Ge_2$, Phys. Rev. Mater. **1**, 044404 (2017).

[14] A. P. Dioguardi, P. Guzman, P. F. S. Rosa, N. J. Ghimire, S. Eley, S. E. Brown, J. D. Thompson, E. D. Bauer, and F. Ronning, Nuclear magnetic resonance investigation of the heavy fermion system $Ce_2CoAl_7Ge_4$, Phys. Rev. B **96**, 245132 (2017).

[15] N. J. Ghimire, S. K. Cary, S. Eley, N. A. Wakeham, P. F. S. Rosa, T. Albrecht-Schmitt, Y. Lee, M. Janoschek, C. M. Brown, L. Civale, J. D. Thompson, F. Ronning, and E. D. Bauer, Physical properties of the $Ce_2MAl_7Ge_4$ heavy-fermion compounds (M = Co, Ir, Ni, Pd), Phys. Rev. B **93**, 205141 (2016).

[16] P. C. Canfield and Z. Fisk, Growth of single crystals from metallic fluxes, Philos. Mag. B **65**, 1117 (1992).

[17] O. V. Dolomanov, L. J. Bourhis, R. J. Gildea, J. A. K. Howard, and H. Puschmann, OLEX2: A complete structure solution, refinement and analysis program, J. Appl. Crystallogr. **42**, 339 (2009).

[18] A. L. Spek, Single-crystal structure validation with the program PLATON, J. Appl. Crystallogr. **36**, 7 (2003).

[19] M. Avdeev and J. R. Hester, ECHIDNA: A decade of high-resolution neutron powder diffraction at OPAL, J. Appl. Crystallogr. **51**, 1597 (2018).

[20] C.-M. Wu, G. Deng, J. S. Gardner, P. Vorderwisch, W.-H. Li, S. Yano, J.-C. Peng, and E. Imamovicc, SIKA—The multiplexing cold-neutron triple-axis spectrometer at ANSTO, J. Inst. **11**, P10009 (2016).

[21] S. Yano, G. N. Iles, J.-Ch. Peng, and Ch.-M. Wu, Current status of the Taiwanese cold triple axis spectrometers, SIKA, at ANSTO, J. Surf. Invest.: X-Ray, Synchrotron Neutron Tech. **14**, S207 (2020).

[22] L. B. McCusker, R. B. Von Dreele, D. E. Cox, D. Louër, and P. Scardi, Rietveld refinement guidelines, J. Appl. Crystallogr. **32**, 36 (1999).

[23] J. Rodríguez-Carvajal, Recent advances in magnetic structure determination by neutron powder diffraction, Phys. B (Amsterdam, Neth.) **192**, 55 (1993).

[24] S. V. Gallego, E. S. Tasci, G. de la Flor, J. M. Perez-Mato, and M. I. Aroyo, Magnetic symmetry in the Bilbao Crystallographic Server: A computer program to provide systematic absences of magnetic neutron diffraction, J. Appl. Crystallogr. **45**, 1236 (2012).

[25] J. M. Perez-Mato, S. V. Gallego, E. S. Tasci, L. Elcoro, G. de la Flor, and M. I. Aroyo, Symmetry-based computational tools for magnetic crystallography, Annu. Rev. Mater. Res. **45**, 217 (2015).

[26] See Supplemental Material at http://link.aps.org/supplemental/10.1103/PhysRevB.107.214435 for bond lengths, bond angles, the check CIF/PLATON report, and the EDX report for $Pr_2PdAl_7Ge_4$.

[27] A. Maurya, R. Kulkarni, A. Thamizhavel, and S. K. Dhar, Anisotropic physical properties of $PrRhAl_4Si_2$ single crystal: A non-magnetic singlet ground state compound, Solid State Commun. **240**, 24 (2016).

[28] F. Gao, W. J. Ren, Y. X. Zhuang, X. G. Zhao, B. Li, and Z. D. Zhang, Magnetocaloric effect in antiferromagnetic $ErAl_2Ge_2$ single crystal, J. Magn. Magn. Mater. **533**, 168014 (2021).

[29] S. Legvild, *Handbook of Magnetic Materials* (Academic, Ames, 1980), Vol. 1, p. 206.

[30] R. J. Elliott and F. A. Wedgwood, Theory of the resistance of the rare earth metals, Proc. Phys. Soc. **81**, 846 (1963).

[31] T. Takabatake, M. Shirase, K. Katoh, Y. Echizen, K. Sugiyama, and T. Osakabe, Superzone gap formation in UCu_2Sn, J. Magn. Magn. Mater. **177-181**, 53 (1998).

[32] T. Onimaru, Y. F. Inoue, K. Shigetoh, K. Umeo, H. Kubo, R. A. Ribeiro, A. Ishida, M. A. Avila, K. Ohoyama, M. Sera, and T. Takabatake, Giant uniaxial anisotropy in the magnetic and transport properties of $CePd_5Al_2$, J. Phys. Soc. Jpn. **77**, 074708 (2008).

[33] P. K. Das, N. Kumar, R. Kulkarni, S. K. Dhar, and A. Thamizhavel, Anisotropic magnetic properties and superzone gap formation in CeGe single crystal, J. Phys.: Condens. Matter **24**, 146003 (2012).

[34] S. Manni, A. Thamizhavel, and S. K. Dhar, Investigation of structural and magnetic properties of $PrIr_3B_2$ single crystal, AIP Adv. **9**, 035021 (2019).

[35] P. Peratheepan and A. M. Strydom, Electronic, magnetic, and transport properties of the isotypic aluminides SmT_2Al_{10} (T = Fe, Ru), J. Phys.: Condens. Matter **27**, 095604 (2015).

[36] T. Tsutaoka, K. Obata, A. A. Sherstobitov, E. G. Gerasimov, P. B. Terentev, and N. V. Baranov, Magnetic order, phase transitions and electrical resistivity of Ho_7Rh_3 single crystals, J. Alloys Compd. **654**, 126 (2016).

[37] M. Matin, R. Mondal, A. Thamizhavel, A. Provino, P. Manfrinetti, and S. K. Dhar, Single crystal growth and anisotropic magnetic properties of $HoAl_2Ge_2$, AIP Adv. **8**, 055709 (2018).

[38] M. Nandi, A. Thamizhavel, and S. K. Dhar, Anisotropic magnetic properties of trigonal $ErAl_2Ge_2$ single crystal, J. Phys.: Condens. Matter **32**, 185803 (2020).

[39] K.-W. Chen, Y. Lai, Y.-C. Chiu, S. Steven, T. Besara, D. Graf, T. Siegrist, T. E. Albrecht-Schmitt, L. Balicas, and R. E. Baumbach, Possible devil's staircase in the Kondo lattice CeSbSe, Phys. Rev. B **96**, 014421 (2017).

[40] E. F. Bertaut, Representation analysis of magnetic structures, Acta Crystallogr., Sect. A **24**, 217 (1968).

[41] J. Mareschal, J. Sivardiere, G. F. D. Vries, and E. F. Bertaut, Magnetic ordering of terbium in some perovskite compounds, J. Appl. Phys. **39**, 1364 (1968).

[42] I. Plaza, E. Palacios, J. Bartolome, S. Rosenkranz, C. Ritter, and A. Furrer, Neutron diffraction study of $NdScO_3$ below 1 K magnetic structure and hyperfine enhanced polarization of Nd, Phys. B (Amsterdam, Neth.) **234-236**, 635 (1997).

[43] R. Bidaux and P. Meriel, Neutron diffraction study of the nuclear and magnetic structure of $DyAlO_3$, J. Phys. (Paris) **29**, 220 (1968).

[44] K. Knížek, Z. Jirak, P. Novak, and C. de la Cruz, Non-collinear magnetic structures of $TbCoO_3$ and $DyCoO_3$, Solid State Sci. **28**, 26 (2014).

[45] L. S. Wu, S. E. Nikitin, M. Brando, L. Vasylechko, G. Ehlers, M. Frontzek, A. T. Savici, G. Sala, A. D. Christianson, M. D. Lumsden, and A. Podlesnyak, Antiferromagnetic ordering and dipolar interactions of $YbAlO_3$, Phys. Rev. B **99**, 195117 (2019).

[46] N. Zhao, J. M. Sheng, J. C. Wang, H. Ge, T. T. Li, J. Yang, S. M. Wang, P. Miao, H. He, X. Tong, W. Bao, E.-J. Guo, R. Mole, D. H. Yu, A. A. Podlesnyak, and L. S. Wu, Quasi-one-dimensional Ising-like antiferromagnetism in the rare-earth perovskite oxide $TbScO_3$, Phys. Rev. Mater. **7**, 034401 (2023).